

Techniques for the Generation and Detection of Picosecond Pulses and Their Applications

Himanshu Aggrawal, Peiyu Chen, M. Mahdi Assefzadeh, Babak Jamali and Aydin Babakhani
Rice University, Houston, USA 77005

I. INTRODUCTION

The technology for generation, modulation, radiation, detection, and demodulation of electromagnetic waves has significantly evolved over the last 120 years. In early 1890s, Guglielmo Marconi used a spark-gap transmitter to build a wireless telegraphy system. In his design, he charged a first capacitor to a high DC voltage and connected it to a parallel combination of an inductor, a second capacitor, and an antenna. In this configuration, when the DC voltage of the first capacitor reaches the breakdown voltage of the gap, the air in the gap ionizes and reduces the resistance across the gap. This results in a large step voltage applied to the parallel combination of the inductor, second capacitor, and the antenna. This mechanism converts the DC energy stored in the first capacitor to a damped oscillation at a low MHz range which is radiated from the antenna. In his design, Marconi used the spark-gap as a fast high-voltage switch. The technology for generation of electromagnetic waves was significantly evolved by the invention of vacuum tubes in mid-1920s. Vacuum tubes enabled amplification of oscillatory signals in the MHz range and provided enough bandwidth for transferring audio signals.

With the start of the second world-war, the radar application of electromagnetic waves received a significant attention. Major resources were allocated for developing pulsed radars in the microwave regime to locate war planes by measuring the round-trip travel time of the electromagnetic pulses. In addition, the time-domain signature of the reflected pulses were analyzed to identify the type of the planes. In this application, shorter pulses are required because the reflection of a short pulse from different parts of a plane arrives in different times, making it easier to identify the object.

During the second half of the 20th century, led by the birth of transistors and integrated circuits, the cost of producing electromagnetic signals in the GHz regime was significantly reduced. This resulted in the birth of cellular networks for consumer applications. Due to the None-Line-of-Sight (NLOS) nature of the cellular links and the high frequency-dependency of the NLOS links, the communication channels were separated in the frequency domain to minimize the interference between multiples users. In a rich-scattering NLOS channel, where the bandwidth of a single user is much smaller than the aggregative bandwidth of the entire network, it is easier to separate users in the frequency-domain. This is because a user can filter the signals generated by other users in the frequency-domain and does not need to receive any feedback from other users to demodulate its own signal.

Over the past decade, there has been a significant shift to mm-wave and THz frequencies due the advancements in source/detector technologies and the rapidly rising demand for wireless data [1]–[5]. In addition to high-speed wireless communication, mm-wave and THz frequencies enable many exciting applications such as high-resolution 3D imaging radars for security cameras and driverless cars, miniaturized radars for gesture detection and touch-less smart-phones, spectrometers for explosive detection and gas sensing, precision time/frequency transfer, wireless synchronization of widely-spaced arrays, and secure LOS communication (directional modulation) enabled by joint-coding through widely-spaced transmitters. Fig. 1 illustrates some of these applications.

Electromagnetic waves in the mm-Wave and THz frequencies and their source/detector technologies have several key differences versus their RF and microwave counterparts. First, mm-wave and THz waves experience a high loss in None-Line-Of-Sight (NLOS) environments. mm-Wave and THz transmitters produce a highly directive laser-like beam that travel in a LOS path to a receiver (or to an object) but suffer a high loss in a NLOS channel. Second, due to the small size of the antennas and low power levels, a large number of coherent transmit elements are required to boost the power and increase the effective aperture size while enabling broadband electronic beam-steering. Third, the fundamental oscillators in the mm-wave and THz regimes lack the required frequency stability and suffer from high phase-noise due to the poor efficiency of the gain stages. In order to lock these oscillators to a stable reference signal at a low frequency, a power consuming PLL equipped with many divider stages are required.

In this article, we are reporting multiple source/detector technologies that are capable of producing and detecting ultra-short pulses with duration of few picoseconds. These sources/detectors are ideal for LOS applications such as $>100\text{Gbits/sec}$ point-to-point communication, 3D imaging radars, and gas spectroscopy. The picosecond source technology [6] can produce frequency-comb reaching 1THz, which is five times higher than the fT of transistor used in the design. The produced THz tones have a line-width of better than 2Hz that can be used for precision time/frequency transfer and localization. The generated picosecond pulses have a timing jitter of better than 200 femtosecond enabling depth sensing with accuracy of 60um or better. The detector is designed to capture the picosecond pulses with an on-chip antenna and extract the amplitude of the pulses and their repetition frequency enabling wireless synchronization of a mm-wave array.

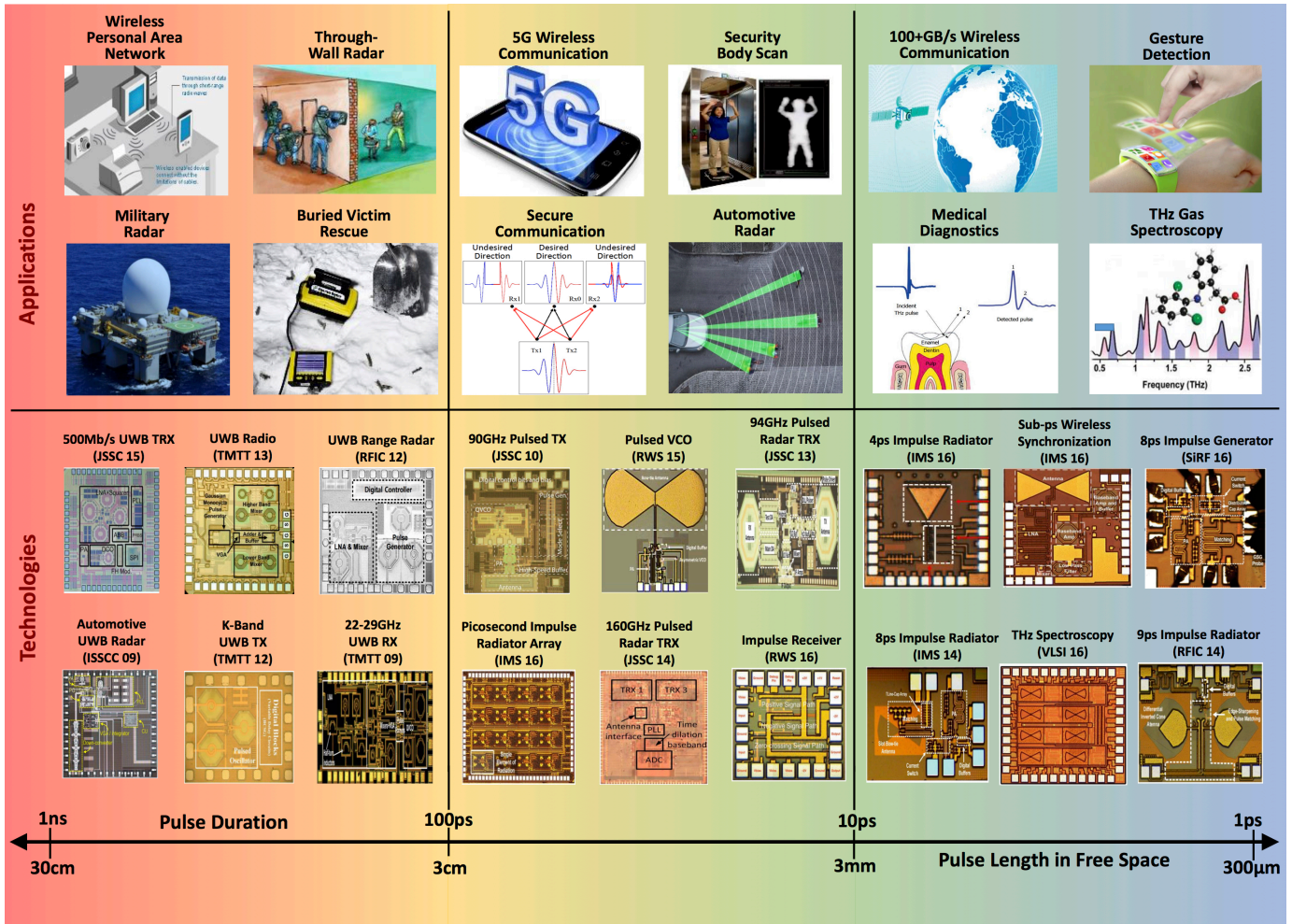


Fig. 1. mm-Wave and it's applications (JSSC 15 [7], TMTT 13 [8], RFC12 [9], ISSCC 09 [10], TMTT 12 [11], TMTT 09 [12], JSSC 10 [13], RWS 15 [14], JSSC 13 [15], IMS 16 [16], JSSC 14 [17], RWS 16 [18], IMS 16 [19], IMS 16 [20], SiRF 16 [21], IMS 14 [22], VLSI 16 [6], IMS 14 [?])

In addition to reporting several source/detector technologies, we will demonstrate how pulse-based systems are used to produce high-resolution 3D images and enable secure wireless communication.

II. SOURCES

A. Laser-Based Techniques

Picosecond pulses are traditionally generated with a femtosecond laser and a photoconductive antenna (PCA). The procedure is to bias two electrodes of a PCA with a DC voltage, thereby generating an electric field on a semiconducting material. Although no current flows in the absence of optical illumination, an ultra-short (~ 100 femtosecond) optical pulse generates electrons and holes, which produce a current due to the electric field. Because of the small transition region (a few microns) and the short transport time, this technique can generate sub-picosecond pulses. As illustrated in Fig. 2, the short impulse current generates broadband picosecond radiation with frequencies reaching 1 THz.

Broadband radiation can be detected by a similar method. The spectroscopy based on this method of applying a femtosecond laser with source/detector PCAs is referred to as Terahertz Time Domain Spectroscopy (THz-TDS). THz-TDS offer several disadvantages. It requires a bulky laser that costs tens of thousands of dollars and requires time-consuming optical alignment. The laser has a low repetition rate (< 100 MHz),

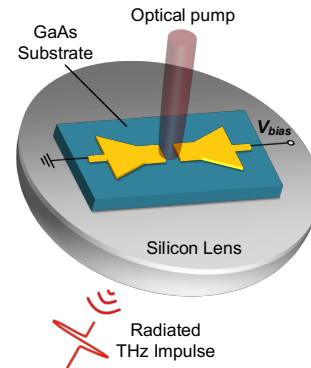


Fig. 2. THz impulse radiation with a femtosecond laser and a PCA

which translates into low average radiated power (~ 1 W). THz-TDS is a single-source, single-detector method that provides no beam-steering capability; to generate images, one must move the object mechanically. To capture an entire pulse, the system requires a mechanical delay line to add delay in the optical path to vary the time of the sampling. The slow speed of the mechanical delay line translates into a slow acquisition speed. To overcome these disadvantages, a laser-free, fully electronic way to generate picosecond pulses is required.

B. Laser-free Fully Electronic Terahertz Sources

To conduct THz spectroscopy and generate high-resolution 3D radar images, ultra-short pulses with broad frequency spectra are required. Several recent publications have reported silicon-based broadband signal radiation with coherent pulses shorter than 50 picoseconds. Two main pulse-generation architectures have been proposed.

Oscillator-based CW Designs: Impulses can be generated by switching voltage-controlled oscillators (VCOs). However, simply switching a conventional VCO that has a symmetric topology will induce phase-ambiguity problems. To alleviate this, an asymmetric cross-coupled VCO is proposed [14]. The proposed VCO topology can generate impulses that have a deterministic starting phase and are locked to the input trigger. In an asymmetric cross-coupled pair, the size of one transistor is larger than the other, which creates a deterministic initial condition rather than a random one that is mostly contributed by thermal noise. A prototype chip is implemented in a 130nm SiGe BiCMOS process technology with a 30GHz asymmetric VCO and on-chip antennas (Fig. 3). The chip can radiate impulses with a minimum full-width-at-half-maximum of 60 picosecond. The radiated impulse has a RMS jitter of 178fsec, when an input trigger with a jitter of 150 femtosecond is used. Fig. 4 demonstrates the impulse spatial combining by using two widely spaced impulse radiators. The measured combined impulse waveform is almost identical to the algebraic summation of the two impulses radiated by the two individual impulse radiators.

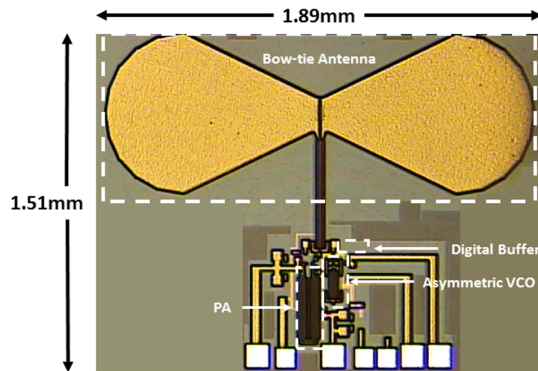


Fig. 3. Chip micrograph of oscillator-based impulse generator

Direct Digital to Impulse: An 8psec impulse radiator was reported in 2014 that is based on an oscillator-less *Direct Digital to Impulse* (D2I) architecture. In this design, a magnetic

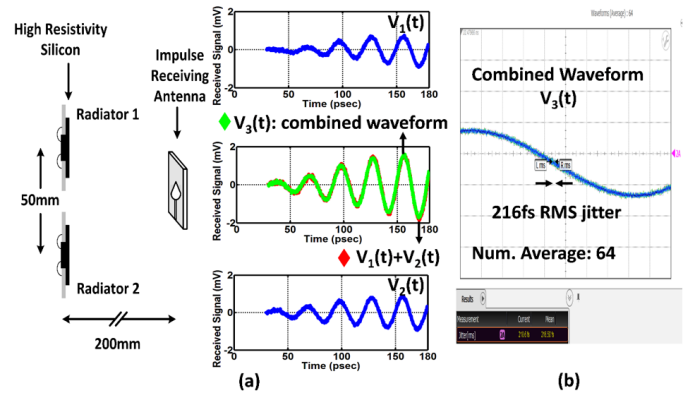


Fig. 4. Coherent spatial pulse combining of two widely spaced radiators

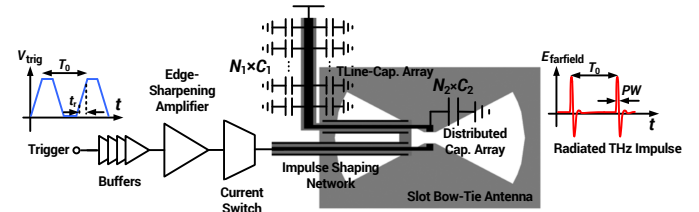


Fig. 5. Schematic of the digital-to-impulse radiator

energy is being stored in a broadband phase-linear antenna carrying a DC current. A fast current switch abruptly releases the stored magnetic energy, transferring the rising/falling edge of a digital input trigger into an impulse radiation.

Fig. 5 shows a block diagram and schematics of the 8 picosecond impulse radiator with a D2I architecture. In this circuit, a digital trigger signal with a rise time of 120 picoseconds arrives at the input of the chip. A series of digital buffers reduces the rise time of the signal to 30 picoseconds and sends it to a power amplifier for further amplification. A broadband slot bow-tie antenna designed to radiate ultra-short impulses is connected to a bipolar switch. When the switch is on, a DC current energizes the antenna; when the power amplifier turns off the switch, the current stored in the antenna radiates ultra-short impulses that are coherent with the digital trigger. A transmission-line-based pulse-matching network maximizes the energy of each impulse while minimizing its duration. Fig. 6 reports 8psec pulses radiated by the chip and Fig. 7 shows a micrograph of the chip, which occupies an area of $0.55\text{mm} \times 0.85\text{mm}$ and is fabricated in a 130nm SiGe BiCMOS process. The chip radiates impulses with peak Effective Isotropic Radiated Power (EIRP) of 20 mW.

The D2I architecture offers several key advantages over oscillator-based CW designs:

- The broadband pulse covers a wide range of frequencies, making it an ideal candidate for THz spectroscopy and 3D radar imaging.
- The starting time of the impulse synchronizes with the rise time of the input trigger signal. The starting time of the radiated impulse can be controlled by delaying the

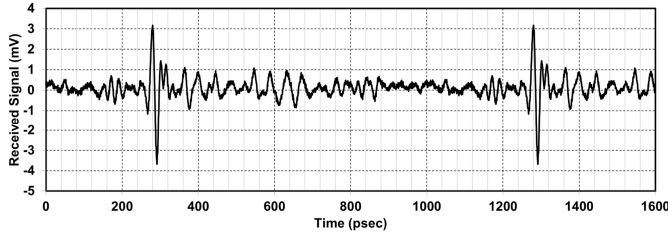


Fig. 6. Time-domain waveform of 8ps radiated pulse

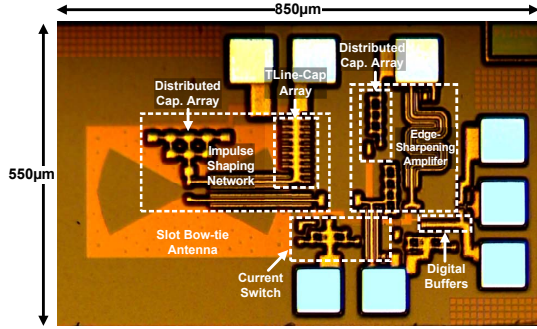


Fig. 7. Chip micrograph of digital-to-impulse radiator

trigger signal. This unique characteristic delivers a major advantage by making it possible to achieve broadband beam steering with arrays of these devices by delaying the trigger signal. In this design, all frequency components of the pulses experience exactly the same time delay.

- When a stable low-frequency clock generates the trigger signal periodically, the radiated signal forms an impulse train with a repetition frequency that equals the clock frequency, resulting in a frequency-comb spectrum suitable for broadband THz spectroscopy.

In order to increase the radiated power and gain beam steering capability, an array of impulse radiator is proposed. An aperture created by a coherent impulse radiator array with N -elements can improve the received power by a factor of N^2 . Moreover, the point where all the pulses combine coherently can be changed by merely changing the delays on each radiator. As shown in Fig. 8, a 4×4 array was fabricated where the impulse from each element coherently combined in air [16]. In this 4×4 array, a single trigger signal is fed to chip and routed to 16 radiators in an H-Tree scheme. In addition, a digitally-programmable delay block is used at each element to provide align the radiated pulses in the space with accuracy of 200 femtosecond. This chip produces 14 picosecond pulses with peak EIRP of 17dBm. The chips was implemented in a 65nm bulk CMOS process technology and occupies an area of xxxmm by xxxmm.

To reduce the duration of the radiated pulses to 4 picosecond, the technique of nonlinear Q-switching impedance (NLQSI) is reported in [19]. In this method, the NLQSI element passes the positive pulse to the antenna but, to avoid ringings and reduce the pulse duration, it changes the quality-factor of the tank when the pulse becomes negative. This

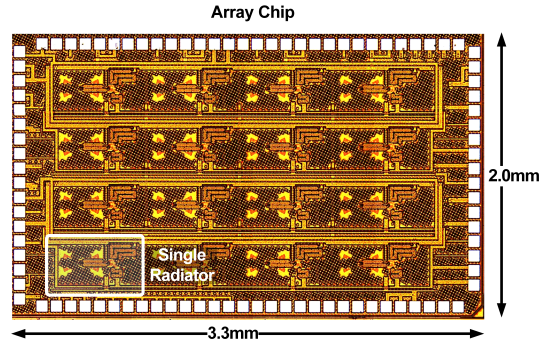


Fig. 8. Chip micrograph of digital-to-impulse radiator array

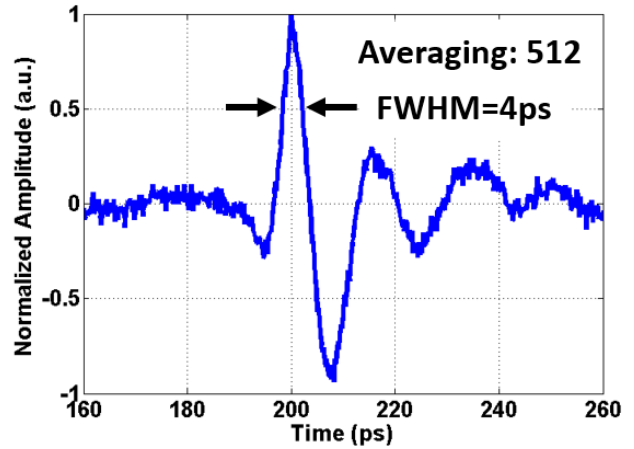


Fig. 9. Raw time-domain waveform of 4ps impulse

method enables generation and radiation of impulses with Full-Width-at-Half-Maximum (FEHM) of 4 picosecond. Figure Fig. 9 shows the time-domain pulses radiated by the chip measured by a novel laser-sampling method. The impulse radiator in can radiate 4picosecond pulses with $\text{SNR} > 1$ bandwidth of more than 160GHz (Fig. 10). This chip allows amplitude reconfiguration capability using a four-way on-chip inductive impulse combining scheme. The chip is fabricated in a 130nm SiGe BiCMOS process and occupies an area of 1mm^2 .

In order to increase the power and reduce the duration of the radiated pulses, a 4×2 SiGe BiCMOS D2I chips is reported in [6]. The chips is equipped with a programmable delay block at each elements and radiates pulses with FWHM of 5.4 picosecond and peak EIRP of 1W. Fig. 11 shows a micrograph of the chip. The chip is fabricated in a 90nm SiGe BiCMOS technology and occupies an area of xxxmm \times xxxmm.

III. DETECTORS

A. High-speed Sampling with Optical Methods

Currently, the only way to sample a picosecond signal is via photoconductive detection with a femtosecond laser and a PCA, as illustrated in Fig. 12. The laser produces 100-femtosecond optical pulses to generate electron-hole pairs with a short ($\sim 1\text{psec}$) lifetime at the center of the PCA.

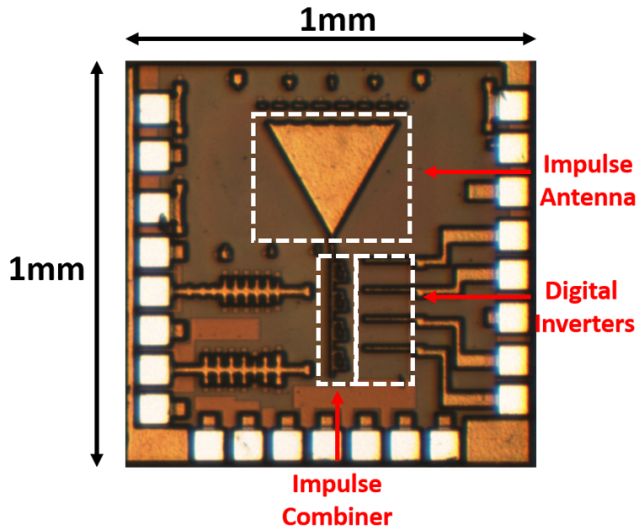


Fig. 10. Chip micrograph of 4ps impulse radiator with pulse amplitude modulation capability

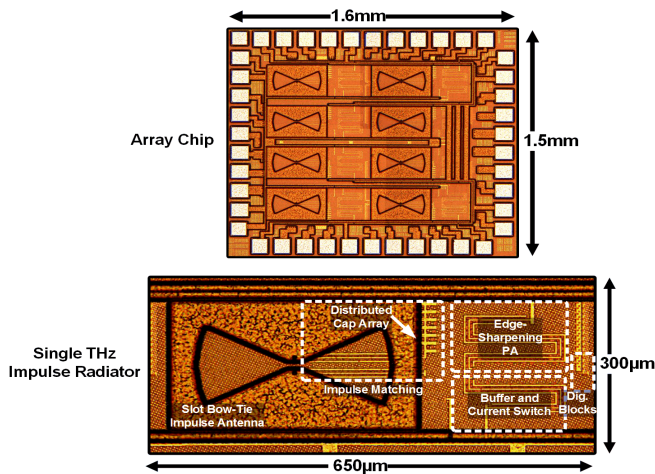


Fig. 11. Chip micrograph of 5.4ps impulse radiator in SiGe BiCMOS

These electron-holes pairs interact with the electric field of the incoming wave to generate DC current. Since the lifetime of the electron-holes pairs is ~ 1 picosecond, they can support a picosecond sampler. Although these systems have a large effective bandwidth (hundreds of GHz), the repetition rate of the femtosecond laser (< 100 MHz) limits their sampling rate. Thus the technique of sampling picosecond THz pulses with a femtosecond laser and a PCA is a subsampling method. Furthermore, these systems require an expensive laser, sensitive optical alignment, and a mechanical delay line to scan a sampling time with steps smaller than 100 femtosecond.

B. Laser-free Fully Electronic Samplers

High-speed Sampler: A silicon based ultra-wideband sampler operating at 100's of GHz is an ideal receiver for pulse-based systems. However, it is extremely difficult to design and

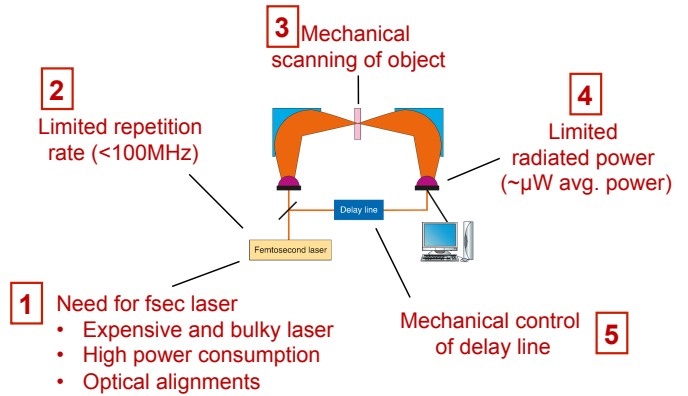


Fig. 12. Limitations of THz-TDS systems

build an ultra-wideband sampler, one of the reason being the parasitic leakages at higher input frequencies and other reasons include the poor efficiency of gain stages in THz frequencies. To address the challenge of parasitic leakage from the input to the holding capacitor, a novel active cancellation technique is reported.

A conventional sample and hold or track and hold architecture uses a transistor as a sampling switch. Ideally, this transistor should have very low impedance in sample/track mode and very high impedance in hold mode. However, at higher input frequencies, the isolation of the sampling transistor decreases rapidly. The parasitic C_{SG} and C_{GD} capacitance provides an additional path for the signal to leak to the holding capacitor. This leakage corrupts the voltage in the holding capacitor and reduces the performance of the sampler. A novel active cancellation architecture was introduced to mitigate this parasitic leakage [23]. In this architecture, a dummy transistor is added in parallel to the sampling transistor. The dummy transistor is always in "OFF" mode and is fed with a signal that is complementary to the input signal. Now during the hold mode, the sampling transistor injects some charge on the holding capacitor due to parasitic leakages; the dummy transistor, fed with a negative copy of the input signal, also injects charge on the holding capacitor. Since, the charge injected by the dummy transistor is negative of that injected by the sampling transistor, they cancel each other and mitigate the parasitic leakage. This is further illustrated in Fig. 13. Fig. 14 shows that the isolation can be increased by > 30 dB at 1GHz by enabling the method of active cancellation. Fig. 15 shows the micrograph of the chip that employs active cancellation to reduce the parasitic leakage from the input to the holding capacitor. The chip was fabricated in a 45nm CMOS-SOI process and occupies an area of 0.13mm^2 .

To address the challenge of sampling 10s of GHz of bandwidth, frequency interleaved sampling architecture have been reported [24], [25]. Even though these samplers are able to operate for broader range of input frequencies, they suffer from a number of challenges, including aliasing, frequency spurious, and down conversion frequency mismatch.

In many applications such as high-speed communication

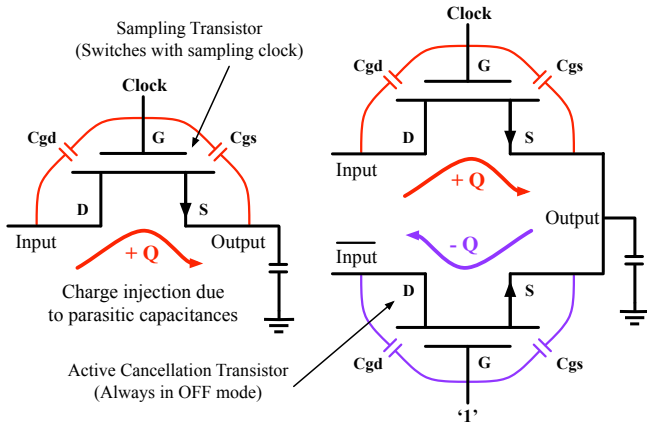


Fig. 13. (Left) Figure shows a conventional sampling switch. Parasitic capacitances C_{SG} and C_{GD} provide an alternate path for the input signal to couple to the sampling capacitor. (Right) Shows a sampling switch with active cancellation. A dummy transistor, which is always off, is added in parallel to the sampling transistor. The parasitic charge dumped by the sampling switch is removed by the canceling transistor.

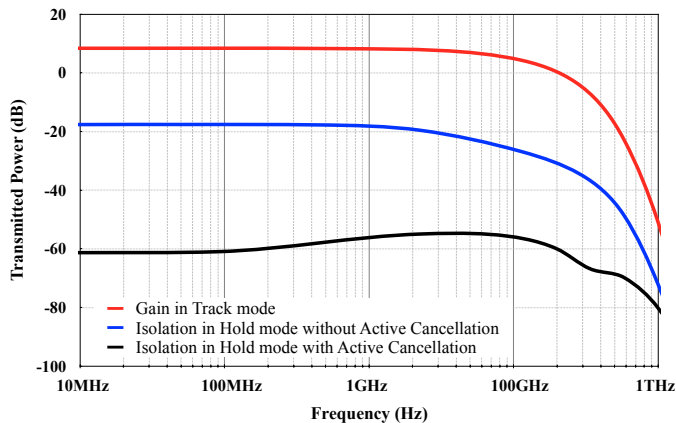


Fig. 14. The simulated isolation between the track and hold modes, with and without the active cancellation block

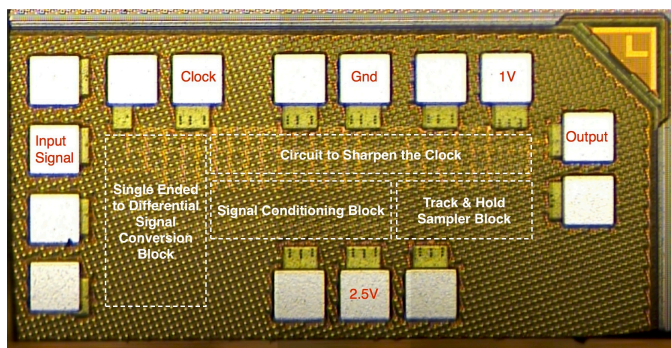


Fig. 15. Chip micrograph of Track-and-Hold Amplifier in 45nm IBM CMOS-SOI node, measuring $850\text{m} \times 450\text{m}$ including pads and 0.12mm^2 without pads

and 3D imaging radars, a picosecond receiver that can measure the energy of the pulse would be very valuable. By measuring the energy of picosecond pulses, it is possible to perform only amplitude modulation and still generate 100Gbits/sec of data. For example, the 4 picosecond pulses reported in [19] can be interleaved in time by using multiple pulse radiators that are synchronized with each-other. By using 10 picosecond spacing between two pulses and adding 2-bits of amplitude modulation, it is possible to generate 200Gbits/sec of information. Energy detectors recover both energy of the pulse and its time of the arrival. These two quantities are needed to build a high-resolution 3D imaging radar as shown in section IV. In addition to wireless communication and imaging radars, energy detectors can be used in a time/frequency transfer systems. In this application, picosecond pulses are radiated with a repetition rate equal to frequency of a clock that needs to be transferred. On the receiver part, an energy detector can be used to generate a clock signal by measuring the repetition rate of the incoming pulse train. Next few paragraphs explain how an energy detector based on self-mixing can be used to extract the repetition frequency of a picosecond impulse train.

Self-Mixing Receiver: An impulse receiver based on a self-mixing technique was reported in [20]. The receiver detects picosecond impulses and extracts their repetition rate with a low timing jitter. Ultra-short pulses captured by the receiving antenna have broadband frequency comb spectra in which the center frequency is determined by the pulse width. The repetition rate of these pulses, fed by a signal source to the transmitter, sets the spacing between every two adjacent frequency tones. When the broadband Gaussian-modulated frequency comb is passed through a nonlinear block, different frequency tones mix with each other and produce the repetition tone at the output. A single bipolar transistor, biased at its most nonlinear region, is used as the mixer. The rest of the architecture includes an input amplifier chain at 50 GHz, a low-pass filter to remove the high-frequency feedthrough, and baseband amplifiers to amplify the main tone of the repetition rate with a tunable center frequency of 1 to 10 GHz. A broadband on-chip bow-tie antenna was also implemented to detect ultra-short pulses. The receiver was fabricated in IBM 0.13m SiGe BiCMOS process and the fabricated chip micrograph is shown in Fig. 16. A custom-designed 8 picosecond pulse-radiating chip, reported in Section II, was used to test the performance of the receiver and the repetition rate of pulses was extracted wirelessly with RMS jitter of 376 femtoseconds.

IV. APPLICATION OF PULSE-BASED SYSTEMS

This section focuses on few applications of pulse-based systems and demonstrates how the pulse sources/detectors can be used to produce high-resolution 3D radar images, detect gas molecules based on THz transmission spectroscopy, establish a secure wireless communication link through joint spatial coding, and finally transfer time with accuracy of 100 femtosecond and measure distance with accuracy of $30\mu\text{m}$.

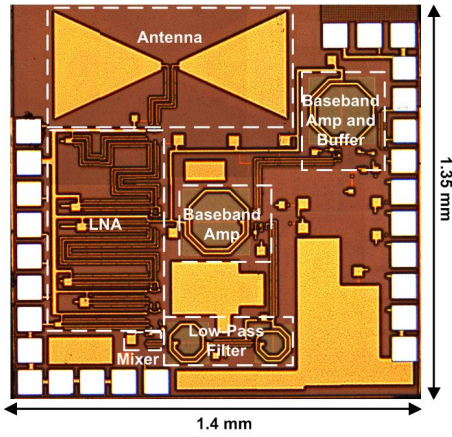


Fig. 16. Chip micrograph of the fabricated impulse receiver

A. 3D Radar Imaging

In a pulse-based imaging system, an array of radar transmitters fire pulses such that they arrive at a desired location in 3D space at the same time. When an object is located in that location, the pulse gets reflected. An array of pulse receivers synchronized with the transmitter array are used to detect those reflections and calculate the location of the object in 3D space on the travel time of the pulses. To demonstrate this concept, a synthetic aperture created by an impulse radiator array with 9×9 -elements. A single radiator is moved to 81 locations, and a sampling oscilloscope connected to a custom PCB antenna is used to capture the reflected impulses from the objects. With grid spacing of 5mm, an effective aperture size of $4\text{cm} \times 4\text{cm}$ is achieved. As shown in Fig. 17, the whole imaging system consists of an impulse-radiating chip, a 2D travel stage, a custom-designed impulse-receiving antenna, and a sampling oscilloscope.

A four-step methodology is proposed to perform 3D imaging by using a synthetic impulse-radiating array. As illustrated in Fig. 18, the synthetic array is on the XY plane.

Capturing Reflected Waveforms: A 2D traveling stage moves the impulse radiator to construct a synthetic array. At the location of each element, the reflected waveforms from the targets are captured by the receiver antenna and then saved for further digital signal processing. After completing data acquisition at a fixed location, the 2D traveling stage moves the impulse radiator to the location of the next element; and then the same data-acquisition operation is performed until a complete synthetic array is formed.

DSP-based Beamforming: The impulses radiated from different elements in the synthetic array travel different distances to a certain point P (x, y, z) in the 3D space. Therefore, the radiated impulses from all elements in the synthetic array can be aligned at point P when the appropriate time delays are added to the radiated impulses. Similarly, because there is only one direct signal path between point P and the receiver antenna, the calculated time delays can also be added to the received waveforms, which results in aligning in time

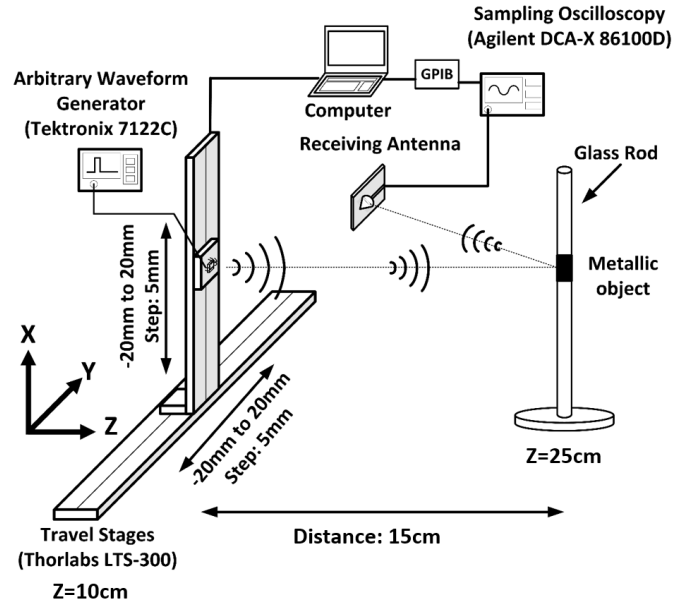


Fig. 17. The custom-designed coherent array 3D imaging system

the information on point P embedded in all of the received waveforms. Adding the properly delayed received waveforms results in a high SNR for waves reflected from point P.

Time-domain Processing: Based on time-of-flight information, the enhanced waveforms reflected from point P are filtered in time and saved. The image-pixel intensity of point P is chosen as the maximum amplitude of the saved waveform. As demonstrated in Fig. 18(c), if there is no object at point P, the image-pixel intensity of point P is a negligible number (noise), because no reflection happens at point P. If there is an object at point P, however, the image-pixel intensity of point P is a large number that is proportional to the reflection coefficient of point P.

Producing 3D Images: As shown in Fig. 18(d), a 2D cross-section can be generated by scanning point P on an image plane, which is defined as a finite XY plane with a fixed Z coordinate. 3D images are generated by varying the value of the Z coordinate of the image plane.

Several objects are used to demonstrate the capability of the 3D imaging array. These objects include a small cylindrical aluminum foil, two spaced cylindrical aluminum foils, and a large ring covered by aluminum foil. The chip emits 60ps impulses with a repetition period of 3ns. The target distance is 25cm ($Z=25\text{cm}$). By post processing the received waveforms from 81 locations, 3D images are generated. As shown in Fig. 19, at $Z=20\text{cm}$, no object is detected. At $Z=25\text{cm}$, which is the exact Z-coordinate of the objects, the produced mm-wave images show the shape of the objects. The 178 femtosecond root of mean square (RMS) jitter of the radiated impulses corresponds to a depth resolution of 27m in the air. Unlike prior art [26], [27], these high-resolution images are produced without using any lenses or reflectors.

The pulse sources in this experiment are based on an

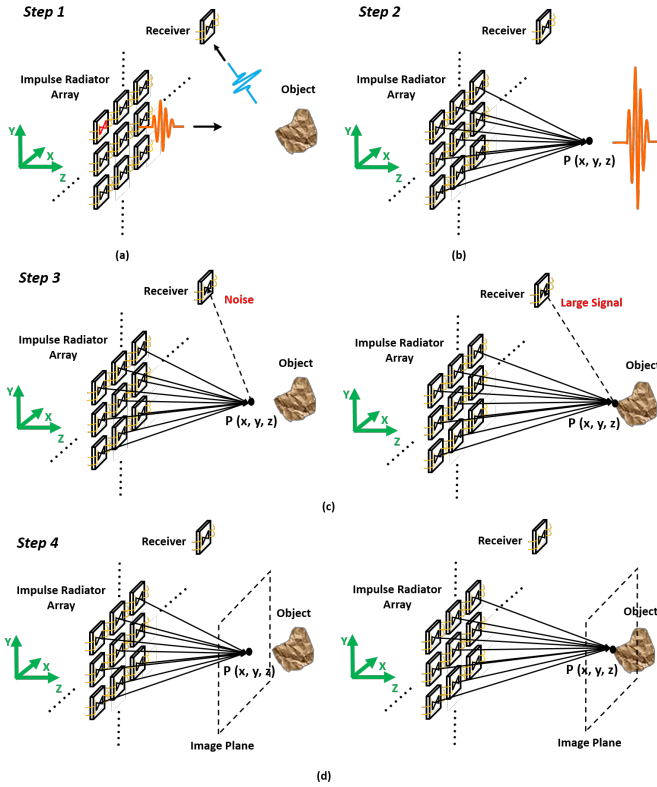


Fig. 18. The proposed 3D imaging methodology

asymmetrical VCO integrated with an on-chip bow-tie antenna that produces pulses with duration of 60 picosecond. A micrograph of this impulse radiator is shown in Fig. 3. The chips was fabricated in a 130nm SiGe BiCMOS process and occupies an area of 2.85mm².

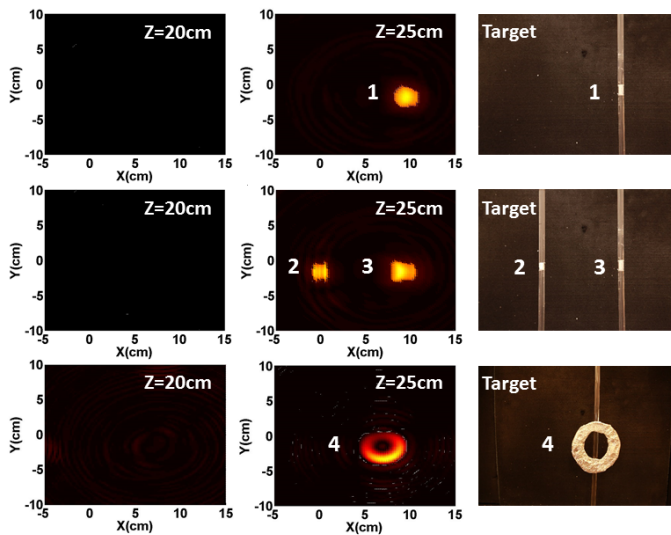


Fig. 19. Captured 3D images of three scenarios

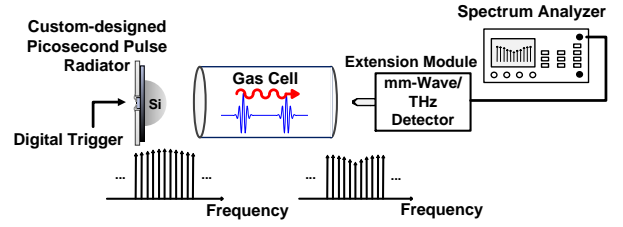


Fig. 20. Proposed terahertz gas spectroscopy setup

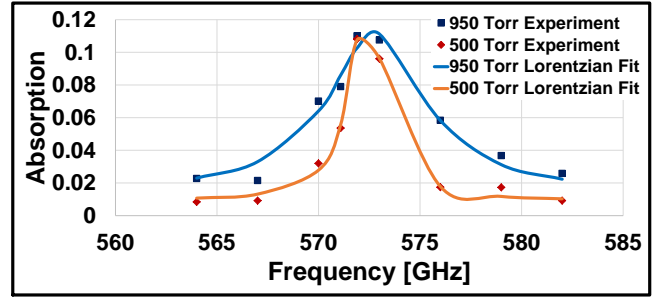


Fig. 21. Measured absorption spectra for Ammonia

B. Spectroscopy

Terahertz spectroscopy using frequency combs has become an effective technique for high-precision detection of gas molecules [28], [29]. This technique can be used to detect the absorption lines in gasses caused by transitions between rotational states in the THz spectral range. The tunability of the terahertz source over a wide range of frequencies with a high resolution enables broadband terahertz trace gas spectroscopy. A laser-free electronic source with an on-chip antenna that can radiate picosecond pulses is used to perform broadband THz gas spectroscopy [30]. Fig. 20 illustrates a setup used for performing terahertz gas spectroscopy. In this experiment 5.4 picosecond pulses are generated by a 4×2 array of D2I radiators shown in Fig. 11. In this experiment, a VDI harmonic mixer WR-1.5 coupled with a Keysight signal analyzer N9030A are used to receive the pulses. Fig. 21 shows the absorption spectrum of Ammonia gas with 1% concentration in two different pressure levels. These results match with the expected absorption line of NH_3 gas at 572 GHz.

C. Pulse-based Secure Communication

In conventional wireless communication systems, information is generated by a single transmitter at a signal location in space. In this case, the information is broadcasted in space, with directionality defined by the directivity of the transmitting antenna. A beam-forming technique is used to concentrate power in a specific region; however, the information is still radiated everywhere in space. An eavesdropper with a sensitive receiver could receive and decode the information. In order to secure the communication channel at the physical layer

(e.g. an antenna level), the concept of Near-Field Direct Antenna Modulation (NF-DAM) or directional modulation were introduced [31]–[33]. In these schemes, the information was jointly generated and broadcasted by different antennas, such that the time-domain signal integrity is preserved at the direction of transmission. This prevents an eavesdropper from capturing the transmitted data outside an *information beam*. In these schemes that utilize joint spatial coding, instead of transmitting complete symbols from an antenna (same symbols from all the antennas in a beam-formed system), semi-symbols are transmitted from multiple antennas such that they combine to form a complete symbol at a specific point in space. The ability to produce symbols at a specific point in space spatially encrypts the communication link.

Joint Spatial Coding: The joint spatial coding architecture uses multiple transmitting antennas tightly synchronized at the symbol level to generate information at a single point in space. A receiver present at this point receives the correct transmitted symbol and can decode the information. For all other points in space, corrupted symbols are received.

The joint spatial coding can be understood from Fig. 22. Let the complete time-domain symbol be represented by $s_{\text{orig}}(t)$. This complete time-domain symbol can be divided into two semi-symbols $s_1(t)$ and $s_2(t)$, such that $s_{\text{orig}}(t) = s_1(t) + s_2(t)$. The signal $s_1(t)$ is generated by the first transmitter (Tx_1), $s_2(t)$ generated by the second transmitter. Let τ_1 and τ_2 be the propagation delays from Tx_1 and Tx_2 to a point P in space, respectively. The signal received at any point in space is given by $s_1(t - \tau_1) + s_2(t - \tau_2)$. A point P in space equidistant from all three transmitters will receive the transmitted signal at the same time, and the signal will be added coherently. The coherent signal addition produces the desired original transmitted signal ($s_{\text{orig}}(t)$). On the other hand, when the point P is not equidistant from all the three transmitters, the signals arrive at different times and produce a distorted time-domain waveform.

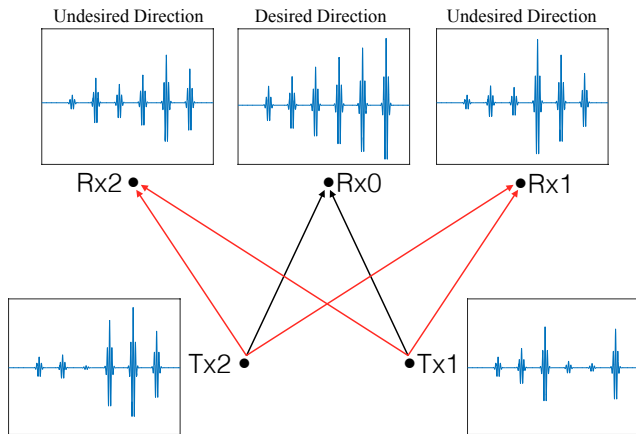


Fig. 22. Pulse-based secure communication

Inspired by the aforementioned joint spatial coding, as shown in Fig. 22, Tx1 and Tx2 transmit a train of amplitude-modulated impulses for a receiver that is equidistant from

all of the transmitter, which then receives the correct data (impulse ramp). For a non-equidistant receiver, however, the received data are corrupted, which makes pulse-based communication spatially secure. In addition, the information beamwidth of this architecture is extremely narrow. As shown in Fig. 23, the information beam is less than 2° .

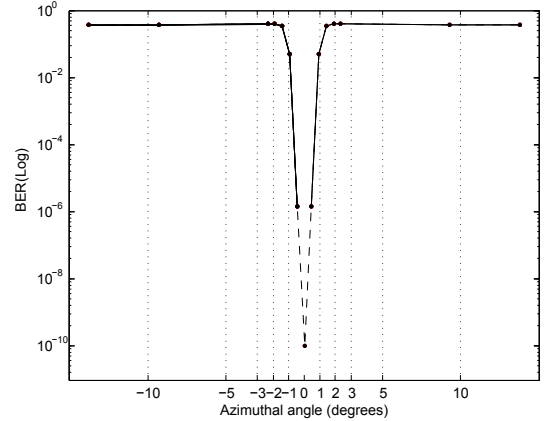


Fig. 23. Bit error rate

D. Precision Time/Frequency Transfer and Localization

Traditionally, an energy detector is used to detect ultra-short pulses. Most energy detectors are diode-based and suffer from multiple drawbacks. Such detectors detect the energy of the input signal irrespective its shape/type, thus making them waveform non-selective. Moreover, the timing accuracy is limited by the pulse width and not pulse jitter, as illustrated in Fig. 24. A waveform selective, zero-crossing detector is proposed that uses the main zero-crossing of the pulse to generate the timing signal [18]. The architecture divides the incoming signal into three paths: the first path detects the rising edge of the pulse, the second path detects the falling edge of the pulse, and the third path detects all the zero-crossings. A high-speed *AND* gate-equivalent circuitry is used to mask all of the false zero-crossings from the main zero-crossing. The BiCMOS chip can detect impulses with a pulse width of 80 picoseconds (FWHM) and with a jitter of less than 100 femtoseconds. Fig. 25 shows the chip micrograph of zero-detector.

V. CONCLUSION

To be written by Aydin

ACKNOWLEDGMENT

Do we need to acknowledge anyone ?

REFERENCES

- [1] K. c. Huang and Z. Wang, "Terahertz terabit wireless communication," *IEEE Microwave Magazine*, 2011.
- [2] G. Fettweis and S. Alamouti, "5g: Personal mobile internet beyond what cellular did to telephony," *IEEE Communications Magazine*, 2014.
- [3] S. Bi, R. Zhang, Z. Ding, and S. Cui, "Wireless communications in the era of big data," *IEEE Communications Magazine*, 2015.

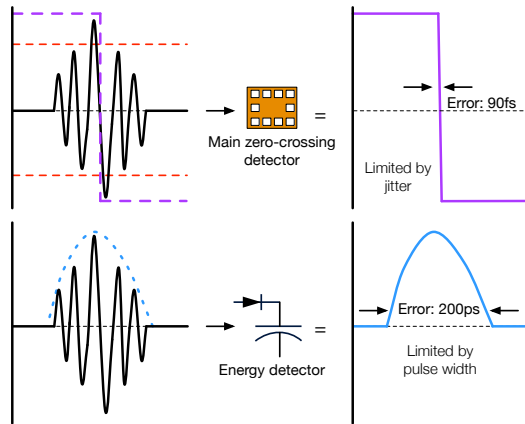


Fig. 24. Energy detector versus main zero-crossing detector

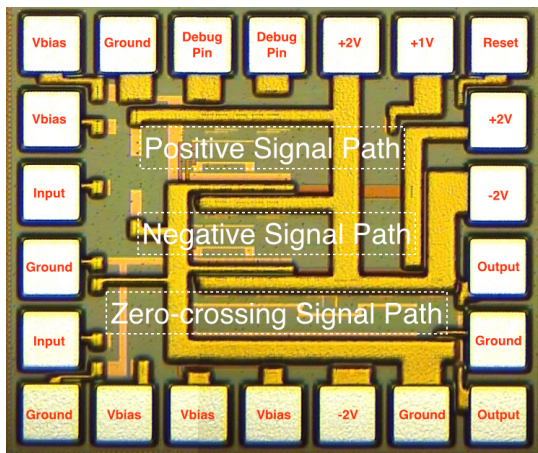


Fig. 25. Energy detector versus main zero-crossing detector

[4] C. Dehos, J. L. Gonzalez, A. D. Domenico, D. Ktnas, and L. Dussopt, "Millimeter-wave access and backhauling: the solution to the exponential data traffic increase in 5g mobile communications systems?" *IEEE Communications Magazine*, 2014.

[5] K. B. Cooper and G. Chattopadhyay, "Submillimeter-wave radar: Solid-state system design and applications," *IEEE Microwave Magazine*, 2014.

[6] M. M. Assefzadeh and A. Babakhani, "Broadband thz spectroscopic imaging based on a fully integrated 4x2 digital-to-impulse radiating array with a full-spectrum of 0.03-1.03thz in silicon," in *IEEE Symposium on VLSI Technology and Circuits*, 2016.

[7] S. Geng, D. Liu, Y. Li, H. Zhuo, W. Rhee, and Z. Wang, "A 13.3 mw 500 mb/s ir-uwband transceiver with link margin enhancement technique for meter-range communications," *IEEE Journal of Solid-State Circuits*, 2015.

[8] H. Hedayati and K. Entesari, "A 90-nm cmos uwb impulse radio transmitter with 30-db in-band notch at ieee 802.11a system," *IEEE Transactions on Microwave Theory and Techniques*, 2013.

[9] S. Lee, S. Kong, C. Y. Kim, and S. Hong, "A low-power k-band cmos uwb radar transceiver ic for short range detection," in *2012 IEEE Radio Frequency Integrated Circuits Symposium*, 2012.

[10] E. Ragonese, A. Scuderi, V. Giammello, E. Messina, and G. Palmisano, "A fully integrated 24ghz uwb radar sensor for automotive applications," in *2009 IEEE International Solid-State Circuits Conference - Digest of Technical Papers*, 2009.

[11] S. Lee, C. Y. Kim, and S. Hong, "A k-band cmos uwb radar transmitter with a bi-phase modulating pulsed oscillator," *IEEE Transactions on Microwave Theory and Techniques*, 2012.

[12] V. Jain, S. Sundaraman, and P. Heydari, "A 22-29-ghz uwb pulse-

radar receiver front-end in 0.18-cmos," *IEEE Transactions on Microwave Theory and Techniques*, 2009.

[13] A. Arbabian, S. Callender, S. Kang, B. Afshar, J. C. Chien, and A. M. Niknejad, "A 90 ghz hybrid switching pulsed-transmitter for medical imaging," *IEEE Journal of Solid-State Circuits*, 2010.

[14] P. Chen and A. Babakhani, "A 30ghz impulse radiator with on-chip antennas for high-resolution 3d imaging," in *2015 IEEE Radio and Wireless Symposium (RWS)*, 2015.

[15] A. Arbabian, S. Callender, S. Kang, M. Rangwala, and A. M. Niknejad, "A 94 ghz mm-wave-to-baseband pulsed-radar transceiver with applications in imaging and gesture recognition," *IEEE Journal of Solid-State Circuits*, 2013.

[16] M. M. Assefzadeh and A. Babakhani, "A fully-integrated digitally-programmable 4x4 picosecond digital-to-impulse radiating array in 65nm bulk cmos," in *2016 IEEE MTT-S International Microwave Symposium (IMS2016)*, 2016.

[17] B. P. Ginsburg, S. M. Ramaswamy, V. Rentala, E. Seok, S. Sankaran, and B. Haroun, "A 160 ghz pulsed radar transceiver in 65 nm cmos," *IEEE Journal of Solid-State Circuits*, 2014.

[18] H. Aggrawal and A. Babakhani, "An ultra-wideband impulse receiver for sub-100fsec time-transfer and sub-30 μ m localization," in *2016 IEEE Radio and Wireless Symposium (RWS)*, 2016.

[19] P. Chen and A. Babakhani, "A 4ps amplitude reconfigurable impulse radiator with thz-tds characterization method in 0.13m size bicmos," in *2016 IEEE MTT-S International Microwave Symposium (IMS2016)*, 2016.

[20] B. Jamali and A. Babakhani, "Sub-picosecond Wireless Synchronization Based on a Millimeter-Wave Impulse Receiver with an On-chip Antenna in 0.13 μ m SiGe BiCMOS," in *2016 IEEE MTT-S International Microwave Symposium*, May 2016.

[21] M. M. Assefzadeh and A. Babakhani, "Picosecond digital-to-impulse generator in silicon," in *2016 IEEE 16th Topical Meeting on Silicon Monolithic Integrated Circuits in RF Systems (SiRF)*, 2016.

[22] —, "An 8-psec 13dbm peak eirp digital-to-impulse radiator with an on-chip slot bow-tie antenna in silicon," in *2014 IEEE MTT-S International Microwave Symposium (IMS2014)*, 2014.

[23] H. Aggrawal and A. Babakhani, "A 40gs/s track-and-hold amplifier with 62db sfd3 in 45nm cmos soi," in *2014 IEEE MTT-S International Microwave Symposium (IMS2014)*, 2014.

[24] Q. Lei, Y. Zheng, and L. Siek, "Analysis and design of high performance frequency-interleaved adc," in *2013 IEEE International Symposium on Circuits and Systems (ISCAS2013)*, 2013.

[25] L. Qiu, Y. J. Zheng, and L. Siek, "Design of frequency-interleaved adc with mismatch compensation," *Electronics Letters*, 2014.

[26] P. N. Chen, P. J. Peng, C. Kao, Y. L. Chen, and J. Lee, "A 94ghz 3d-image radar engine with 4tx/4rx beamforming scan technique in 65nm cmos," in *2013 IEEE International Solid-State Circuits Conference Digest of Technical Papers*, 2013.

[27] A. Tang, G. Virbila, D. Murphy, F. Hsiao, Y. H. Wang, Q. J. Gu, Z. Xu, Y. Wu, M. Zhu, and M. C. F. Chang, "A 144ghz 0.76cm-resolution sub-carrier sar phase radar for 3d imaging in 65nm cmos," in *2012 IEEE International Solid-State Circuits Conference*, 2012.

[28] Y. D. Hsieh, Y. Iyonaga, Y. Sakaguchi, S. Yokoyama, H. Inaba, K. Minoshima, F. Hindle, Y. Takahashi, M. Yoshimura, Y. Mori, T. Araki, and T. Yasui, "Terahertz Comb Spectroscopy Traceable to Microwave Frequency Standard," *IEEE Transactions on Terahertz Science and Technology*, May 2013.

[29] Skryl, AS and Pavelyev, DG and Tretyakov, MY and Bakunov, MI, "High-resolution terahertz spectroscopy with a single tunable frequency comb," *Optics express*, 2014.

[30] M. Assefzadeh, B. Jamali, A. Gluszek, A. Hudzikowski, J. Wojtas, F. Tittel, and A. Babakhani, "Terahertz Trace Gas Spectroscopy Based on a Fully-Electronic Frequency-Comb Radiating Array in Silicon," pp. 1-2, June 2016.

[31] A. Babakhani, D. B. Rutledge, and A. Hajimiri, "Transmitter architectures based on near-field direct antenna modulation," *IEEE Journal of Solid-State Circuits*, 2008.

[32] J. Lavaei, A. Babakhani, A. Hajimiri, and J. C. Doyle, "A study of near-field direct antenna modulation systems using convex optimization," in *Proceedings of the 2010 American Control Conference*, 2010.

[33] A. Babakhani, D. B. Rutledge, and A. Hajimiri, "Near-field direct antenna modulation," *IEEE Microwave Magazine*, 2009.